



**Supporting Information:**

**Development of a Photonic ELection Modulator  
(PELM) for light-mediated pre-sample  
longitudinal and transverse electron beam  
shaping**

Beatrice Matilde Ferrari,<sup>†,‡</sup> Cameron James Richard Duncan,<sup>†</sup> Michael Yannai,<sup>¶</sup>  
Raphael Dahan,<sup>¶</sup> Paolo Rosi,<sup>§</sup> Irene Ostroman,<sup>†</sup> Maria Giulia Bravi,<sup>†</sup> Arthur  
Niedermayr,<sup>¶</sup> Tom Lenkiewicz Abudi,<sup>¶</sup> Yuval Adiv,<sup>¶</sup> Tal Fishman,<sup>¶</sup> Sang Tae  
Park,<sup>||</sup> Dan Masiel,<sup>||</sup> Thomas Lagrange,<sup>‡</sup> Fabrizio Carbone,<sup>‡</sup> Vincenzo Grillo,<sup>§</sup> F.  
Javier García de Abajo,<sup>⊥,#</sup> Ido Kaminer,<sup>¶</sup> and Giovanni Maria Vanacore<sup>\*,†</sup>

<sup>†</sup>*LUMiNaD, Department of Materials Science, University of Milano-Bicocca, Milano,  
20126, Italy*

<sup>‡</sup>*LUMES, École Polytechnique Fédérale de Lausanne, Lausanne, 1015, Switzerland*

<sup>¶</sup>*Department of Electrical and Computer Engineering, Technion, Haifa, 32000, Israel*

<sup>§</sup>*CNR-Nano, Istituto di Nanoscienze Consiglio Nazionale delle Ricerche, Modena, 41125,  
Italy*

<sup>||</sup>*IDES-JEOL, Akishima, Tokyo, 196-8558, Japan*

<sup>⊥</sup>*LICFO-Institut de Ciències Fotoniques, The Bascelona Institute of Science and Technology,  
Castelldefels (Barcelona), 08860, Spain*

<sup>#</sup>*ICREA-Institució Catalana de Recerca i Estudis Avançats, Barcelona, 08010, Spain*

E-mail: giovanni.vanacore@unimib.it

## UTEM setup at UniMib

Figure S1 shows the detailed layout of the Ultrafast Transmission Electron Microscope (UTEM) setup at UniMiB. The TEM used is a JEOL JEM-2100, equipped with both Bright-Field and Dark-Field STEM detectors, along with a Dectris QUADRO direct electron detector, which supports imaging at the low electron counts typical of UTEM experiments. The femtosecond laser source is a Yb-based PHAROS laser from Light Conversion, and the Spatial Light Modulator (SLM) used for laser shaping is a HOLOEYE PLUTO, which modulates only the phase of the laser. The laser repetition rate for these experiments is 300 kHz and the power of the shaped IR beam is 10 mW

In the experiments presented in this paper, an aperture is positioned at the sample plane and two laser branches are in use: one UV branch for photo-generation of the probing electron beam and another branch, shaped by the SLM, to modulate the electron beam itself. The objective of this setup is to demonstrate that transverse electron beam shaping can be achieved at the sample plane.

The ultimate goal of our laboratory, however, extends beyond this preliminary experiment. Future works will place a real sample at the sample plane, and the shaped electron beam will be leveraged to selectively probe specific material excitations. To enable these advanced pump-probe experiments, we are implementing a third laser branch to pump the sample. Optical access to the sample is provided via the Energy-Dispersive X-ray (EDX) port, which includes a leaded glass viewport.

## Lens setup and calibration at UniMiB

Under typical operating conditions, the  $C_0$  lens is excited slightly off its resonance voltage to maximize electron collection efficiency. The resonance voltage corresponds to the point at which the electron beam is optimally focused on the phosphor screen, as shown in Fig. S2. The figure shows the electron-beam current density on the phosphor screen as a function of

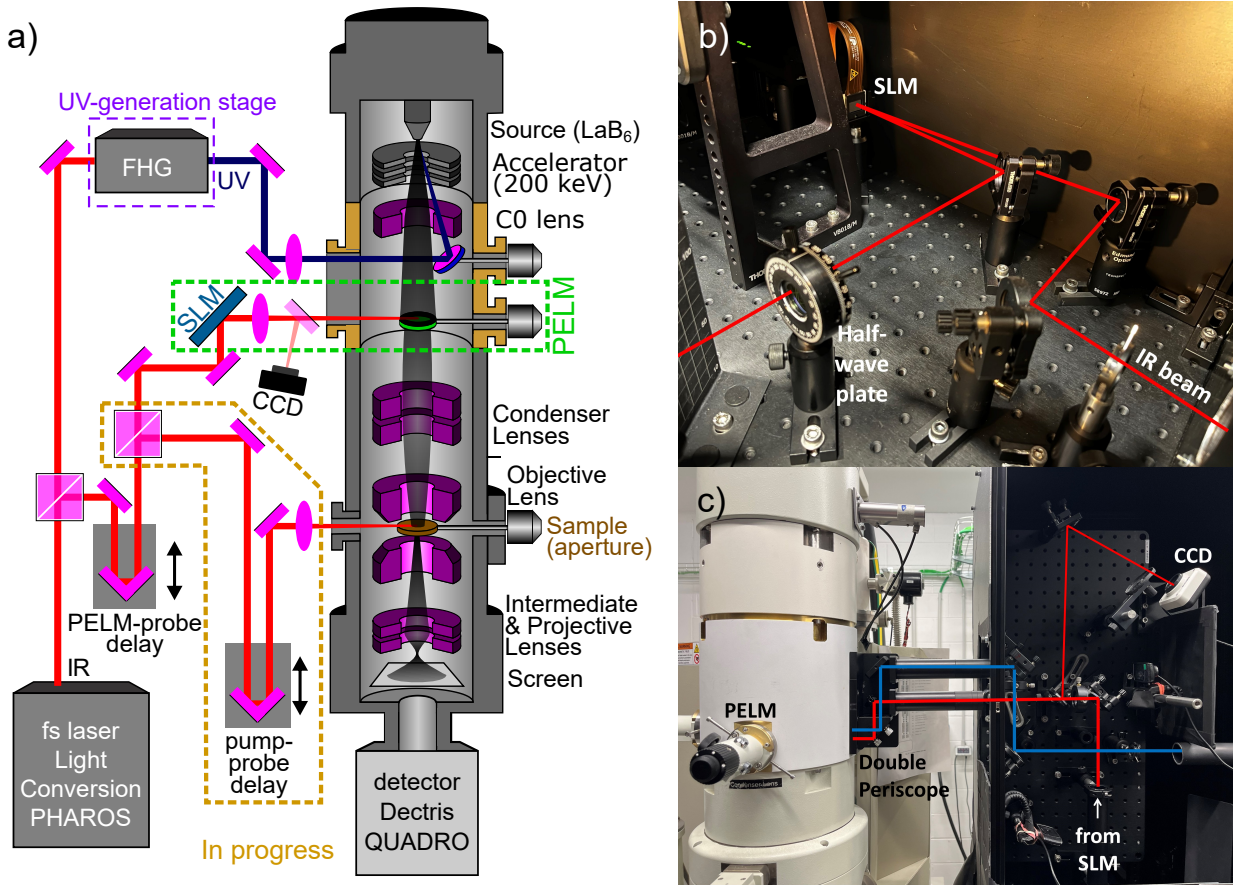


Figure S1: **Detailed layout of the Ultrafast Transmission Electron Microscope (UTEM) setup at UniMiB.** **a)** Schematics. Modified JEOL JEM-2100 TEM equipped with STEM and a Dectris QUADRO detector. A PHAROS femtosecond laser provides UV pulses for photo-generating electron beams and IR pulses shaped by a HOLOEYE PLUTO SLM for transverse electron-beam modulation. An aperture at the sample plane demonstrates shaping, with future plans to replace it with real samples for pump-probe experiments via a third laser branch introduced through the EDX port. **b,c)** Real pictures of our laboratory

$C_0$  lens excitation voltage, with the resonance voltage measured at 23.8 V. To achieve the large coherence needed to resolve Electron Photon Interaction (EPI), the  $C_0$  lens is instead excited only 15 V.

To directly correlate the electron profile between the sample plane and the PELM plane, we avoid forming crossovers between these two planes. This is achieved by operating the TEM in free lens control, turning off all lenses before the sample plane except for a weakly excited  $C_3$  lens, which results in a minimally demagnified electron beam.

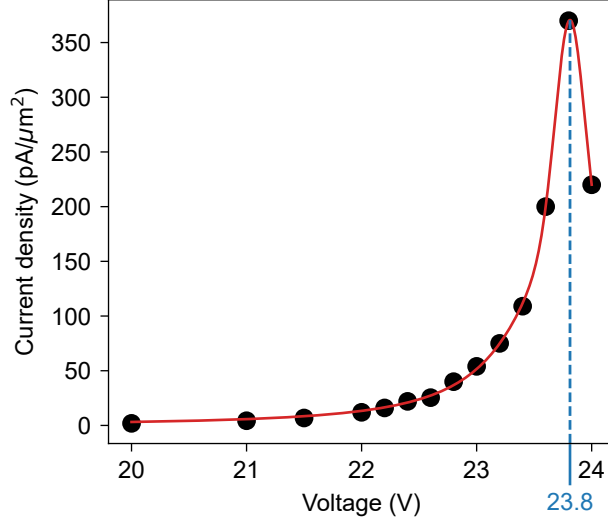


Figure S2: Calibration of the  $C_0$  lens at UniMiB. The electron-beam current density on the phosphor screen is shown as a function of  $C_0$  lens excitation voltage, with the resonance voltage measured at 23.8 V.

Operating the TEM in free lens control also allows us to reach the long Camera Length of 100 m through manual tuning of the intermediate lenses. To establish a momentum scale for our HDD patterns, we place a calibration sample, *latex spheres on diffraction grating replica* (TED Pella product number 673), in the PELM plane. The calibration results are shown in Figure S3.

The resolution per pixel is then calculated as:?

$$1 \text{ pixel} = \frac{\text{grating period } [\mu\text{m}^{-1}]}{\text{peak period } [\text{pixels}]} = \frac{2 \mu\text{m}^{-1}}{0.148} = 0.296 \mu\text{m}^{-1} \quad (1)$$

where the peak period, derived from the diffraction peaks in Figure S3a, is obtained from the Fourier transform shown in Figure S3b.

Using these measurements, we calculate the Camera Length as follows:

$$L_C = \frac{\text{peak period } [\text{pixels}] \times \text{pixel length } [\text{m}]}{\lambda_e [\text{m}] \times \text{grating period } [\text{m}^{-1}]} = 100 \text{ m} \quad (2)$$

where  $\lambda_e \approx 2.5 \text{ pm}$  is the de Broglie wavelength of relativistic electrons at 200 keV.

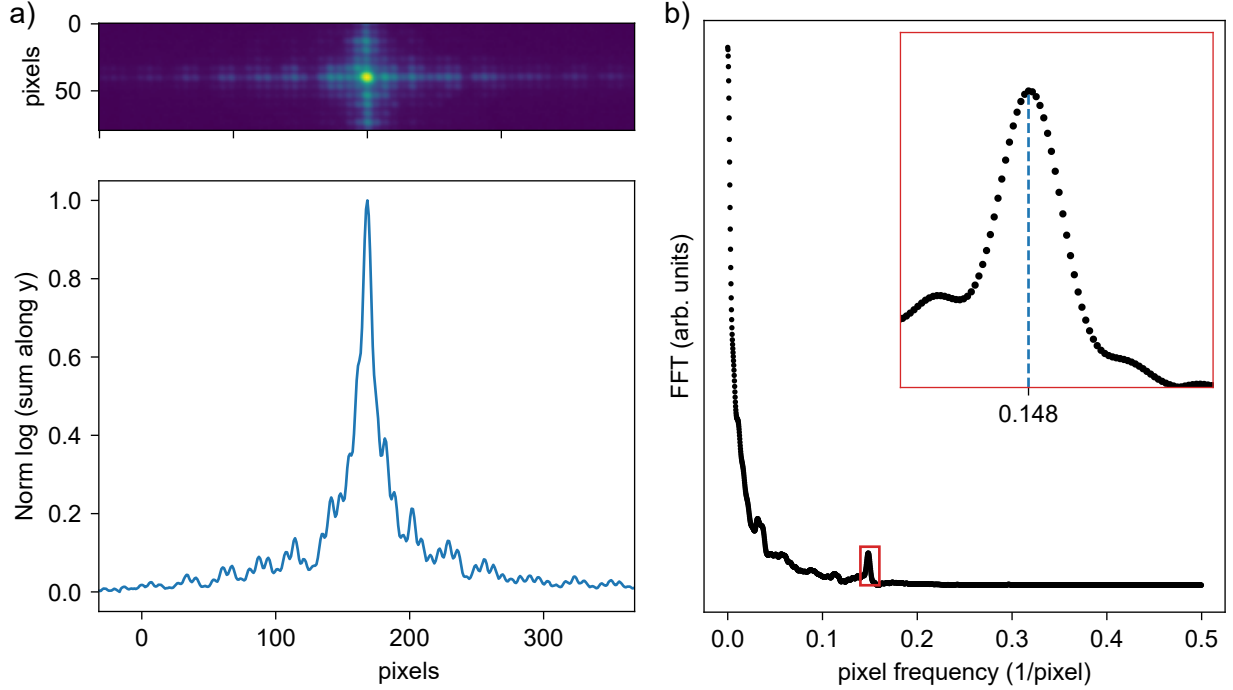


Figure S3: **Calibration of the momentum scale for High Dispersion Diffraction (HDD) patterns.** **a)** Diffraction pattern of the *latex spheres on diffraction grating replica* calibration sample placed at the PELM plane. The grating period is  $2 \mu\text{m}^{-1}$ . **b)** Fourier transform of the diffraction pattern, used to extract the peak period in pixels. From the calibration, we determine that one pixel corresponds to a reciprocal-space value of  $0.296 \mu\text{m}^{-1}$ , and the Camera Length is calculated to be 100 m.

## PELM-membrane geometry and momentum transfer at UniMiB

Figure S4 illustrates the experimental geometry used in our setup, following the layout and labeling convention in Fig. 1 of Ref.<sup>?</sup> and Fig. S1 of Ref.<sup>?</sup> for consistency and ease of comparison. The supplementary materials in these references provide derivations for the membrane-parallel components of the incident light wavevector that are transferred to the electrons during interaction.

In our configuration, the angles  $\theta = 0^\circ$  and  $\delta = 90^\circ$  are fixed (as shown in Fig. S4), while  $\alpha$  is varied to optimize interaction. Using the formula from the supplementary information in Ref.,<sup>??</sup> we calculate the coordinates of the light-wavevector transfer components as:

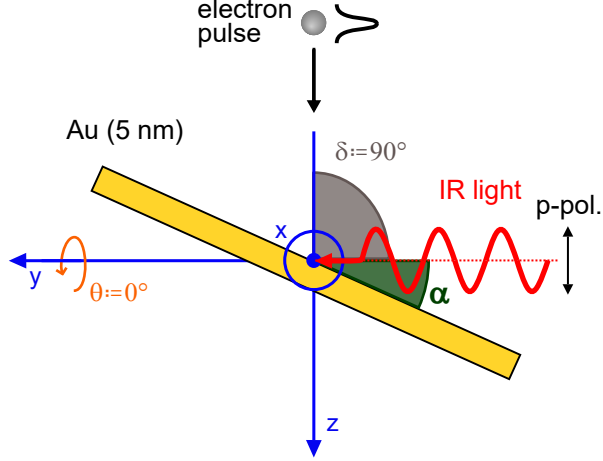


Figure S4: **Experimental geometry of electron-photon interaction (EPI) at the PELM-membrane.** The angles  $\theta$  and  $\alpha$  represent the membrane's rotation around the  $y$ -axis and  $x$ -axis, respectively, relative to the horizontal plane. The angle  $\delta$  specifies the orientation between the electron beam and the light propagation direction. In our laboratory,  $\theta = 0^\circ$  and  $\delta \approx 90^\circ$  are fixed, while  $\alpha$  is adjusted to optimize the interaction. The momentum transfer occurs predominantly along the  $y$  direction, aligned with the laser propagation.

$$q_{L\parallel}(x, y, z) = \left( 0, \cos^2 \alpha, -\frac{\sin 2\alpha}{2} \right) \quad (3)$$

The momentum transferred to the electrons is then given by  $p_L = \frac{\omega}{c} q_{L\parallel}(x, y, z)$ , where  $\frac{\omega}{c}$  is the light wavenumber. As described in the main text, this momentum transfer occurs solely along the laser propagation direction  $y$ .

## Spatial light modulator at UniMiB

The Spatial Light Modulator (SLM) used in this setup is the HOLOEYE Pluto 2.1, which consists of two primary components: (i) a micro-display and (ii) a driver unit. The micro-display comprises a 1920 x 1080 array of liquid crystal on silicon (LCoS) pixels, each measuring  $8 \mu\text{m} \times 8 \mu\text{m}$ . Each pixel can introduce a phase shift in the reflected light, with possible phase shifts ranging from 0 to  $2\pi$ . This phase modulation is optimized for light wavelengths between 650 nm and 1100 nm, ideal for the laser's IR range. When the reflected

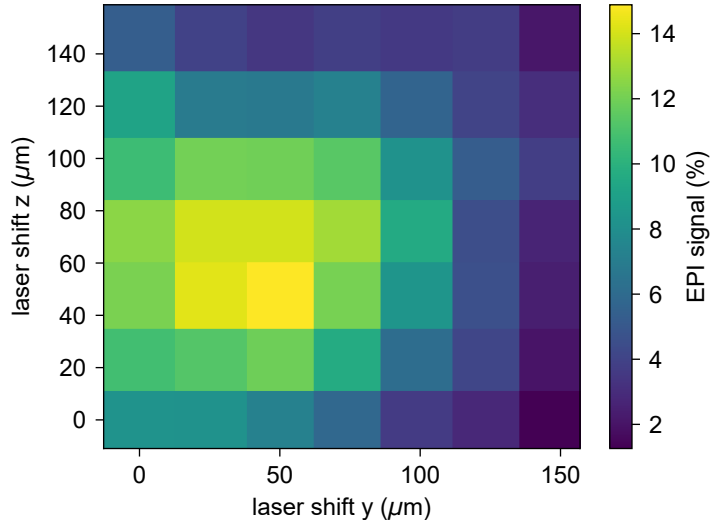


Figure S5: **Two-dimensional laser scan** Pinem signal (see main text) as a function of the laser shift along  $y$  and  $z$ , as defined in Fig. S4.

light propagates through free space, the phase pattern generated by the SLM evolves into an intensity pattern. For optimal performance, the incident laser is set at a  $7^\circ$  angle to the SLM surface and is p-polarized.

The SLM driver unit refreshes the micro-display at a rate of 60 Hz and interfaces with a PC via an HDMI connection. This HDMI connection allows the driver to interpret image data sent from the PC as if the SLM were a standard computer display. Consequently, any software capable of displaying images on a computer monitor can, in principle, control the SLM’s phase pattern. In our experimental setup, a custom Python-based program synchronizes the SLM with the Dectris QUADRO detector, the delay stage, and other components, allowing precise timing and control over beam shaping.

The SLM reflects an unchanged zero-order beam, making the first-order diffracted beam the primary component used for shaping. Consequently, the base pattern applied to the SLM is a blazed diffraction grating, which effectively separates the undesired zero-order (unshaped) beam from the first-order (shaped) beam. When we refer to “using the SLM as a simple mirror”, we are actually describing this configuration, although technically it is not a simple reflection but a diffracted and directed first-order beam.



## 2-Dimensional beam reconstruction at UniMiB

In Fig. 4f of the main text, we show transverse Gaussian modulation of the electron beam along just one spatial coordinate. Nevertheless, we have performed a two-dimensional laser scan as well. This is shown in Fig. S5, further attesting to our ability of full transverse electron shaping.

## UTEM setup at Technion

Figure S6 shows the optical setup at Technion UTEM, which is also described in detail in Ref.<sup>2</sup> Independent laser paths deliver UV light to the TEM cathode and IR light to both the PELM and sample planes. Two delay stages control the relative timing between these three beams, enabling synchronized pump-pump-probe experiments.

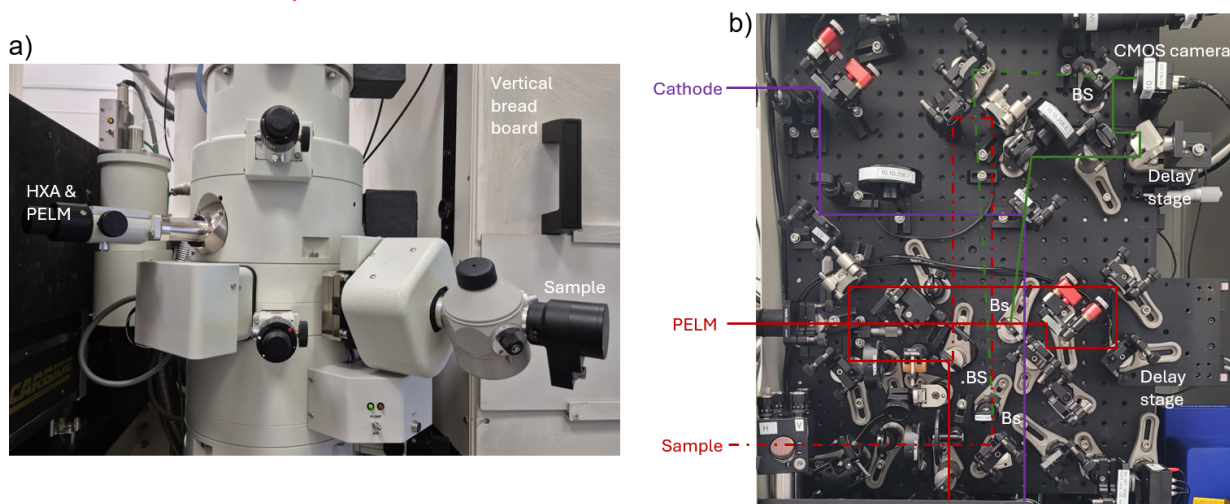


Figure S6: **Optical setup used at Technion UTEM.** a) Image of the microscope column showing the HXA mechanism connected to the PELM (inside the microscope column), the sample, and the vertical bread board (covered by an enclosure, see panel b). b) Detailed layout of the vertical bread board. Three optical access ports are installed on the column allowing the introduction of UV laser light to the TEM cathode (purple path), and adjustable wavelength laser to the PELM (red path) and sample (dot-dashed red path). A delay stage is introduced in the PELM beam path and is used to generate the relative delay between the sample and PELM beams. A small portion of the PELM and sample laser beams is sampled and used to measure their relative phase stability via an optical interferometer (green paths). BS – 50:50 Beam splitter, Bs – Beam sampler (90:10).

# Simulation of the e-beam properties at the pre-CL and post-CL planes

In this section we will present electron trajectory calculations using the software STEM-CELL<sup>??</sup> for simulating the beam characteristics at the pre-CL stage and at the post-CL stage.

For PELM we need an interaction point that – by an electron optics point of view – plays the same role of one of the apertures. The different positions are shown in Fig. S7, which represents the configuration of a JEOL microscope with the addition of a C0 lens and the drift sector.

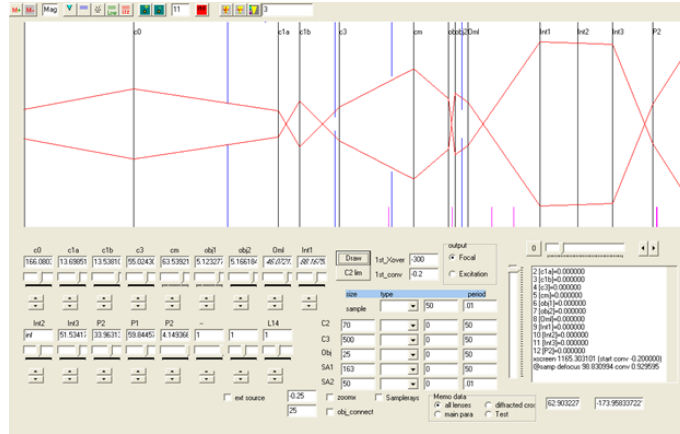


Figure S7: Lens diagram of a JEOL microscope: c0 is the additional condenser lens as discussed in the previous chapters; c1a, c1b and c3 form the condenser lens system; cm is the condenser minilens; obj is the objective lens that surrounds the sample; oml is the objective minilens; Int1, Int2 and Int3 are the intermediate lenses; p2 is the projective lens.

In the scheme, the first aperture is the pre-CL PELM interaction point (apertures are shown in blue in Fig. S7). The third aperture is the standard condenser aperture (CA). In between them, we marked also a fixed aperture of 1-mm size. The HXA aperture is also visible above the condenser minilens. The focal lengths and the lens excitation are that of standard operations with a condenser aperture of 100  $\mu\text{m}$ ; the beam size in the pre-CL PELM point is therefore around 100-200  $\mu\text{m}$ .

As described in the main text, coherent transverse electron beam shaping would require,

in principle, a large lateral coherence. In practice, the combination of Boersch effect and a large source size limits the lateral coherence of the electron beam, which is even more severe for a thermoionic source in the case of pulsed emission. Nevertheless, one can always increase the beam coherence but at the expenses of the total intensity. Here, we discuss which of the two PELM positions is more favorable, considering in particular the ability to tune the coherence. In an ideal experiment we should be able to select the best trade-off between intensity and coherence and for some configuration this can be easier than for others.

The main reason for loss of lateral coherence is the finite extension of the source. For a given cathode and density of emission the only way to increase the coherence is by sacrificing beam intensity. The use of an aperture is able to cut away rays very far off the optical axis, consequently reducing the intensity.

The increase of the coherence can be thus seen by back propagating the rays from the aperture to the tip, thus realizing that we are observing only electrons from a selected part of the tip. The standard way to increase coherence is by using the condenser aperture CA, which determines also the convergence. However, there are cases in which this is not entirely true. Figure S8 and S9 below shows that the rays departing from two different points in the source end up in the same area in the CA plane, but in different points in the sample plane. In this specific case there is a negligible demagnification of the source to the sample. More precisely we considered a spherical wave produced by each point of the source and calculated which trajectories intercept the CA. In a more realistic model the emitted waves are very directional. Nevertheless, this model is qualitatively sufficient to describe the main effects.

The conclusion from the above simulations is that when using the CA as the only limiting aperture we have contribution from each part of the source that is imaged completely on the sample. There is an actual negligible demagnification of the source. While experimental conditions might improve beam characteristics due to the intrinsic directionality of emission, this setup lacks mechanisms for direct control over transverse coherence. One of the possible ways to actively control electron beam coherence is to couple two apertures in two sufficiently

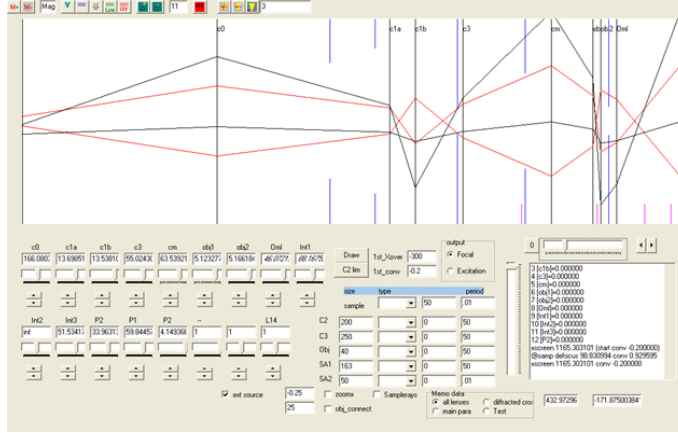


Figure S8: Schematic configuration of lenses where rays departing from two different points in the source end up in the same area in the CA plane, but in different points in the sample plane.

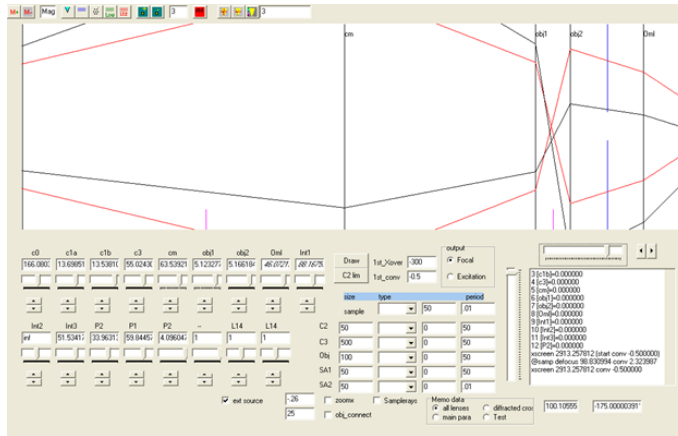


Figure S9: Close-up next to the sample plane of the ray-diagram shown in Fig. S8

different planes. In the ideal case one could use a crossover to cut directly the external rays emitted from the side of the tip, but this is practically impossible as it would require a too small aperture. Still, one of the two apertures must be relatively close to the crossover and the other close to the plane wave condition. This condition can be achieved by using the membrane in the PELM stage as a limiting aperture. The thin membrane used for PELM is electron transparent only within a window of typically  $100 \mu\text{m} \times 100 \mu\text{m}$ , effectively functioning as an aperture. Moreover, additional features, such as smaller circular apertures, can be introduced through techniques like thermal evaporation or focused ion beam (FIB) nanofabrication, enabling finer control over the interaction region.

As an example of how the tandem of the two apertures can work, we show now the case of the CA and the pre-CL PELM. As visible in Fig. S10 below such double aperture system would be able to cut all rays originating from an off-center part of the tip and thus propagating within the column several microns away from the optical axis. These are the most incoherent and aberrated rays of the beam. The way for this to work would be to slightly change the excitation of C1b so that the crossover is set closer to the CA aperture. We can reach smaller and smaller effective size at the cost of the intensity, although requiring smaller and smaller CA and pre-CL PELM aperture. It is worth noticing that even if the beam at the pre-CL PELM aperture is strongly incoherent, the further effect of the CA is able to remove most of the incoherent part of the source rays and rebuild the coherence afterward (at the sample plane).

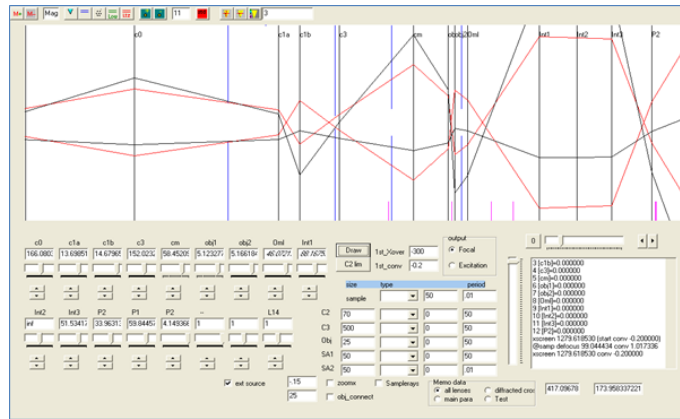


Figure S10: Schematic ray-diagram of the lens system with a pre-CL PELM working in tandem with a condenser aperture CA for post-selection retrieval of electron beam coherence.

The HXA is located after the CA and is hosting the PELM in the post-CL PELM configuration. As shown in Fig. S11, also for this case we can show that we can obtain an effective removal of the rays emitted laterally from the tip, and therefore a tunable increase of the coherence. The main difference here appears to be the size of the beam at the HXA plane, which appears to be a factor 2-3 larger than in the pre-CL PELM position. This feature can be of some advantage in light-mediated beam shaping when the numerical aperture of the illumination system remains low. The exact magnification however would depend on the

details of the excitation of the lenses.

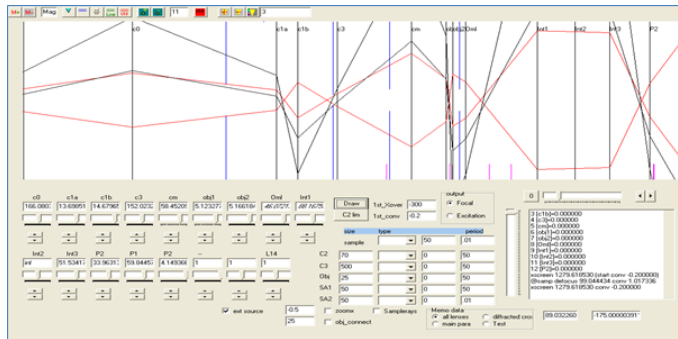


Figure S11: Schematic ray-diagram of the lens system with a post-CL PELM (at the HXA plane) working in tandem with a condenser aperture CA for tunable electron beam coherence.

The pre-CL PELM has many advantages in terms of technical implementation, as it is easy to construct a spatial interaction point and inspect it. Moreover, the additional section allows enough space to be available for all possible configurations and setups. From an electron-optics point of view, coherence of the electron beam can be retrieved when it is used in combination with a condenser aperture. In terms of work flow for experiments, we would need to align it on an intense although incoherent beam (without CA), and then insert CA aperture before measurements. However, if alignment can be done while keeping the CA inserted the effective result of the screen should be similar to the HXA case. The post-CL PELM at the HXA plane offers a larger beam, so the demand for a high numerical aperture illumination scheme can be relaxed. This is however compensated by the difficult geometry that indeed forces to use a limited numerical aperture.

When considering complementarity with the CA for beam control, the post-CL configuration appears to offer a slight advantage compared to the pre-CL case. Specifically, the rejection of the peripheral parts of the beam seems more effective in the HXA plane, although this may depend on the precise lens excitation settings. Furthermore, since the post-CL PELM is positioned after the CA, the electron beam at this stage is already more coherent. This enhanced coherence simplifies alignment and centering during the setup phase, allowing for easier adjustment of the shaping aperture.

In summary, both configurations—pre-CL and post-CL PELM—demonstrate comparable efficacy. The choice between them depends on the specific details of the PELM design and the experimental requirements, with each offering unique advantages.

# Realization of a Pre-Sample Photonic-based Free-Electron Modulator in Ultrafast Transmission Electron Microscopes

Beatrice Matilde Ferrari,<sup>†,‡</sup> Cameron James Richard Duncan,<sup>†</sup> Michael Yannai,<sup>¶</sup> Raphael Dahan,<sup>¶</sup> Paolo Rosi,<sup>§</sup> Irene Ostroman,<sup>†</sup> Maria Giulia Bravi,<sup>†</sup> Arthur Niedermayr,<sup>¶</sup> Tom Lenkiewicz Abudi,<sup>¶</sup> Yuval Adiv,<sup>¶</sup> Tal Fishman,<sup>¶</sup> Sang Tae Park,<sup>||</sup> Dan Masiel,<sup>||</sup> Thomas Lagrange,<sup>‡</sup> Fabrizio Carbone,<sup>‡</sup> Vincenzo Grillo,<sup>§</sup> F. Javier García de Abajo,<sup>⊥, #</sup> Ido Kaminer,<sup>¶</sup> and Giovanni Maria Vanacore<sup>\*,†</sup>

<sup>†</sup>*LUMiNaD, Department of Materials Science, University of Milano-Bicocca, Milano, 20126, Italy*

<sup>‡</sup>*LUMES, École Polytechnique Fédérale de Lausanne, Lausanne, 1015, Switzerland*

<sup>¶</sup>*Department of Electrical and Computer Engineering, Technion, Haifa, 32000, Israel*  
<sup>§</sup>*CNR-Nano, Istituto di Nanoscienze Consiglio Nazionale delle Ricerche, Modena, 41125, Italy*

<sup>||</sup>*IDES-JEOL, Akishima, Tokyo, 196-8558, Japan*

<sup>⊥</sup>*LICFO-Institut de Ciències Fotoniques, The Bascelona Institute of Science and Technology, Castelldefels (Barcelona), 08860, Spain*

<sup>#</sup>*ICREA-Institució Catalana de Recerca i Estudis Avançats, Barcelona, 08010, Spain*

E-mail: giovanni.vanacore@unimib.it

## Abstract

Spatial and temporal light modulation is a well-established technology that enables dynamic shaping of the phase and amplitude of optical fields, significantly enhancing the resolution and sensitivity of imaging methods. Translating this capability to electron beams is highly desirable within the framework of a transmission electron microscope (TEM) to benefit from the nanometer spatial resolution of these instruments. In this work, we report on the experimental realization of a photonic-based free-electron modulator integrated into the column of two ultrafast TEMs for pre-sample electron-beam shaping. Electron-photon interaction is employed to coherently modulate both the transverse and longitudinal components of the electron wave function, while leveraging dynamically controlled optical fields and tailored

design of electron-laser-sample interaction geometry. Using energy- and momentum-resolved electron detection, we successfully reconstruct the shaped electron wave function at the TEM sample plane. These results demonstrate the ability to manipulate the electron wave function before probing the sample, paving the way for the future development of innovative imaging methods in ultrafast electron microscopy.

## Introduction

In recent years, electron-photon interaction (EPI) in Ultrafast Transmission Electron Microscopes (UTEMs) has been extensively adopted as a powerful tool for studying ultrafast dynamics of laser-triggered nanoscale phenomena.<sup>1–12</sup> Lately, there has been a growing interest in transferring well-established laser



modulation techniques to the electron beam (e-beam) of UTEMs. In these experiments, pre-shaped laser fields transfer their modulation to the e-beam through EPI.<sup>13,14</sup> Several approaches, such as optical parametric amplification (OPA),<sup>15</sup> two-wave mixing,<sup>16</sup> as well as dielectric laser acceleration (DLA),<sup>17</sup> have been employed for longitudinal (energy-time) modulation of the electron wave packet, whereas spatial light modulators (SLMs),<sup>18,19</sup> nanoconfined near fields,<sup>20,21</sup> and Fabry-Pérot optical cavities<sup>22</sup> have been used for transverse (momentum-space) shaping of the e-beam.

Two different approaches have been explored for e-beam modulation via light fields: elastic and inelastic interactions. Elastic EPI, mediated by the ponderomotive force,<sup>19,23,24</sup> offers the advantage of not requiring a physical interface to mediate the interaction. However, this method is constrained by the need for high laser intensities and is limited to phase-only modulation (unless two-color illumination is used to produce stimulated Comptons scattering). In contrast, inelastic EPI has been successfully used to modulate both the phase and amplitude of e-beams. A first step in that direction has been taken by exploiting the Photon-Induced Near-field Electron Microscopy (PINEM) approach<sup>25-27</sup> for e-beam shaping.<sup>20,21</sup> In PINEM, the interaction is mediated by the near field generated in the vicinity of a nanostructure (such as a surface plasmon polariton), allowing direct mapping of the structure's complex optical field onto the transverse distribution of the electron wave function. While this one-to-one correspondence is valuable for studying the near-field evolution, it limits the flexibility in e-beam shaping: predicting the final electron distribution requires numerical simulations to account for the near-field effects of the structure, limiting the range of patterns that can be imprinted on the e-beam.

To overcome these limitations, stimulated Inverse Transition Radiation (ITR)<sup>28-30</sup> has emerged as a versatile alternative form of EPI.<sup>18,31-35</sup> Transition radiation (TR) is the electromagnetic wave emitted by an electron passing through an interface between two media with different refractive indices. This ra-

diation is emitted to preserve the continuity of electromagnetic fields at the interface.<sup>36</sup> In the inverse process (i.e., ITR), a stimulating electromagnetic field is already present, and the electron exchanges energy and momentum with such a field in a quantized manner. As a result, ITR allows for direct transfer of the laser phase onto the electron wave function without the near-field contribution present in PINEM, making the final e-beam profile effectively a Fourier transform of the SLM pattern used to shape the laser.<sup>37</sup>

Recently, Madan *et al.*<sup>18</sup> demonstrated electron modulation mediated via inelastic EPI based on ITR using light pre-shaped by an SLM. In that work, the interaction was still occurring at the sample plane, where the film used to mediate ITR was placed. Nevertheless, the authors foresaw a future technological implementation of a pre-sample Photonic-based free-Electron Modulator (PELM). This would be done by adding a new EPI interaction point in a pre-sample stage along the TEM column. Different types of modulation can be then achieved by exploiting the multiplicity of phase patterns that can be imprinted on the SLM, as well as by replacing the SLM itself with other laser shaping technologies, such as optical cavities, DLAs, OPAs, leveraging both spatially and temporally modulated light fields for controlling the e-beam in its multidimensional phase space before reaching the sample.

Realizing such potentials will allow us to use pre-shaped e-beams to selectively probe nanomaterial dynamics with enhanced spatiotemporal resolution and sensitivity to specific properties and degrees of freedom. For instance, shaped electrons could be adopted to selectively probe low-frequency excitations in materials,<sup>35,38,39</sup> to enable low-dose imaging of sensitive scatterers,<sup>37</sup> as well as to enhance image resolution<sup>24</sup> and increase contrast<sup>15</sup> when interrogating materials showing very subtle changes, thus greatly expanding the capabilities of UTEMs.

In this work, we present the experimental implementation of a PELM integrated into two UTEM systems: one at the University of Milano-Bicocca (UniMiB) and the other at the

Israel Institute of Technology (Technion). Both setups were modified to position the PELM before the sample, although at different locations along the TEM column. At UniMiB, the PELM utilizes a SLM for transverse e-beam modulation, while at Technion, a non-collinear OPA (NOPA) is used for longitudinal modulation. By monitoring the electron wave function in its multidimensional phase space (energy, time, space, and momentum), we demonstrate both transverse and longitudinal pre-sample modulation of the e-beam, driven by an externally-controlled light field.

## Results and discussion

### Electron-photon interaction and coherence

As described above, our PELMs exploit ITR to facilitate EPI. In this process, electrons inelastically interact with a strong coherent light source, absorbing and emitting an integer number of photons.<sup>40</sup> This quantized interaction imprints distinct peaks in the electron distribution, corresponding to multiples of the photon's energy and momentum.<sup>29–31,33,34,41</sup>

To resolve these interaction peaks, and hence the quantized nature of EPI, the e-beam energy (or momentum) spread must be narrower than the photon's energy (or momentum). Such narrow spreads are achieved when the e-beam longitudinal (or transverse) coherence length exceeds the wavelength of the interacting photons.<sup>42</sup> This is because the longitudinal and transverse coherence lengths directly determine the e-beam spread in energy and momentum, respectively, when averaging over the electron ensemble of wave functions.<sup>43</sup> It is important to notice that, if the coherence length exceeds the photon wavelength but remains on the same order of magnitude, it is still possible to detect EPI; however, the interaction peaks will be smeared out and the quantum nature of EPI hidden.

In the energy domain, EPI is detected if the temporal coherence of the e-beam is longer than or on the order of an optical cycle. This con-

dition is easily achieved thanks to the small energy spread that results from the photoemission process at the cathode.<sup>44</sup> As a consequence, the electron pulse has a temporal coherence  $\xi_t \approx 5 - 10$  fs, which is greater than the optical cycle (in our case,  $\tau = \lambda/c \approx 3.4$  fs).<sup>42</sup>

In contrast, detecting EPI in the momentum domain is more challenging. In this case, the electron transverse coherence must be greater than or on the order of the laser wavelength. Typical values of transverse coherence for thermionic electron sources, such as those used in our laboratories, are on the order of tens of nanometers,<sup>45,46</sup> which is not enough for experiments with visible and infrared (IR) light. Therefore, particular microscope settings need to be used to increase the beam transverse coherence, as discussed below.

For e-beam shaping, it is crucial not only to achieve sufficient e-beam coherence but also to achieve coherent EPI, since preserving the phase information is critical for advanced imaging techniques. Coherent EPI occurs when the e-beam interacts with a homogeneous portion of the laser's electric field. For longitudinally coherent EPI, the laser pulse is stretched in time to exceed the duration of the electron pulse.<sup>31,33</sup> For transversely coherent EPI, the e-beam spot size is made smaller than the laser spot size.<sup>33</sup>

### Technical Implementation of the PELM device

To realize EPI, we implement a pump-probe scheme. An IR laser pulse, produced by an Yb-based amplified femtosecond laser, is split in two branches. One pulse is up-converted to ultraviolet (UV) light by a 4th harmonic generation stage and is directed to the TEM cathode, inducing photoemission and creating the probing electron pulse. The other pulse is synchronized with the electron pulse and pre-shaped via the SLM. The two pulses interact via ITR on a light-reflective, electron-transparent metallic film at the PELM plane, where the structured laser field imprints its modulation onto the electron wave function. To maximize EPI, the shaped laser pulse is p-polarized with respect to the PELM film.<sup>18</sup>

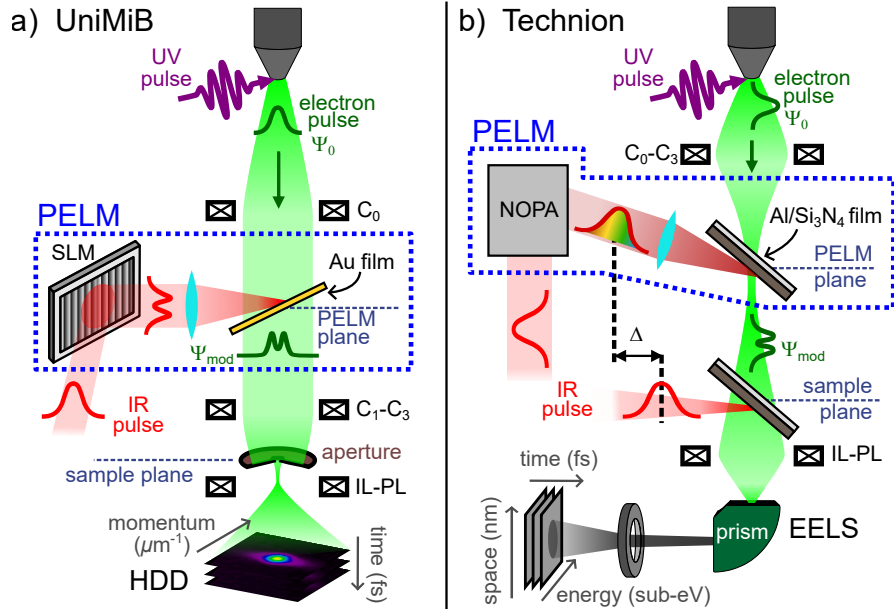


Figure 1: **Schematics of experimental setups incorporating the Photonic Electron Modulator (PELM) in two ultrafast TEM configurations** at University of Milano-Bicocca (UniMiB) (a) and the Israel Institute of Technology (b). **a) Transverse electron-beam shaping at UniMiB.** A Spatial Light Modulator (SLM) is used to shape the transverse laser profile, which is then focused on a thin gold film positioned in a pre-condenser-lens (pre-CL) stage inside the TEM. Femtosecond electron pulses generated by UV laser pulses interact with the modulated IR laser pulses at the PELM-film surface via stimulated inverse transition radiation (ITR). A 20- $\mu\text{m}$  aperture selectively samples a small portion of the modulated e-beam. High Dispersion Diffraction (HDD) patterns of the selected electrons are recorded. By scanning the aperture or laser, the entire transverse electron profile is reconstructed, mimicking 4D-STEM methodologies. **b) Longitudinal electron-beam shaping at Technion.** A Non-collinear Optical Parametric Amplifier (NOPA) is used to tune the optical cycle of the upper laser pulse, which is then directed onto a thin aluminum film deposited on a  $\text{Si}_3\text{N}_4$  membrane located at the Hard X-ray Aperture (HXA) position, between the condenser and objective lenses. The electron pulses are modulated via ITR at the PELM stage. The longitudinal electron modulation is then probed via a double EPI scheme with additional ITR interaction point at the sample plane.

The technical implementation of a PELM device requires integrating two pre-sample access ports to the TEM column reaching the same inner position: an optical port for the modulating laser beam and a micromanipulator to adjust the stage holding the PELM film. This setup must satisfy two main design constraints: (i) sufficient lateral and vertical space within the column to accommodate the PELM film, and (ii) adequate transverse coherence of the e-beam to enable EPI detection. Here, we devise two configurations for integrating the PELM within UTEM setups, each with unique advantages and trade-offs.

Figure 1a shows the UTEM setup at UniMiB,

with more details provided in the Supporting Information (SI). This setup is based on a modified JEOL JEM-2100 TEM operating at 200 keV and equipped with a direct electron detector. The microscope column has been modified to accommodate two additional column sections before the  $C_1$ - $C_3$  condenser lenses (CLs). The upper section houses a supplementary condenser lens, labeled  $C_0$ , while the lower section hosts: a single optical port for both UV and IR beams, an aluminum mirror to guide the UV beam toward the cathode, and the micromanipulator holding the PELM film (see Fig. S1).

Because of its pre-CL position, the PELM at UniMiB offers the key advantage of control-

ling the light-shaped e-beam via the CLs before reaching the sample. This pre-CL shaping is essential for implementing advanced imaging techniques that require, for instance, demagnification of the modulated e-beam at the sample.<sup>37</sup> However, achieving optimal transverse coherence at this pre-CL stage is challenging; under typical imaging conditions, this is generally accomplished by demagnification with the CLs and transverse beam selection with the condenser aperture. Here, to reach the coherence required for resolving EPI at the pre-CL PELM plane, we substantially reduce the excitation voltage of the  $C_0$  lens (see SI) and we use the PELM stage itself as an aperture. Consequently, the e-beam diameter significantly exceeds that of the laser, resulting in substantial loss of useful electron flux, as many electrons fall outside the laser interaction region.

Figure 1b illustrates the UTEM setup at Technion<sup>15</sup> (a real picture is also shown in Fig. S6), based on a modified JEOL JEM-2100Plus TEM operating at 200 keV and equipped with a Gatan Image Filter and a K2 direct electron detector. This configuration includes a single additional column section with: the  $C_0$  lens, the aluminum mirror for the UV beam, and the UV optical port. In this setup, the PELM film is accommodated by modifying the Hard-X-Ray aperture (HXA), located between the condenser and objective lenses. The IR-beam access to the PELM stage is provided through an optical port on the opposite side of the column, with an entrance angle of  $20^\circ$  relative to the horizontal plane.

At Technion, an optical pump line to the sample is implemented by further splitting the IR beam in two paths (see panel b of Fig. S6 in SI). One path is directed to the sample plane via a zero-angle port, while the other enters the microscope at the PELM port, after passing through a fine-delay line.

With respect to the pre-CL configuration implemented at UniMiB, the advantages of the post-CL configuration at Technion are: (i) a lower complexity in terms of technical design and practical realization, because the standard configuration of a TEM column is already designed to host a HXA; and (ii) a higher e-beam

transverse coherence, which is ensured by the CL system. The latter aspect has been qualitatively investigated via electron trajectory calculations using the STEM-CELL software<sup>47,48</sup> (see related section in the SI).

However, such post-CL PELM is limited by the tighter space available in this portion of the column, thus suffering from a lower flexibility in controlling the modulated e-beam before the sample and therefore limiting its versatility.

## Pre-sample electron beam shaping

Having discussed the technical design of the PELM devices, we now proceed to demonstrate their ability to control the e-beam properties within their multidimensional phase space.

### Transverse modulation

Transverse modulation of the e-beam requires modifying both the spatial and momentum coordinates of the single-electron wave function. This can be achieved using spatially structured optical fields. In our case, we employ an SLM to shape the light field, but alternative approaches, such as nanoconfined near fields or photonic cavities, could serve a similar purpose.

At UniMiB, we achieve light-induced transverse e-beam modulation by exploiting inelastic EPI via ITR, which is mediated by a 5-nm thick gold film at the PELM plane. This thickness is not sufficient to approximate the PELM film with a perfect mirror, given that the skin depth of gold is around  $t = \lambda / (2\pi \sqrt{\epsilon_2/2}) \approx 27$  nm, where  $\lambda = 1030$  nm is the wavelength of our laser. Using the approach outlined in the SI of Ref. 31, we simulated the strength of EPI as a function of the PELM film tilt angle  $\alpha$  (as shown in the inset of Fig. 2a), accounting for the non-ideal mirror conditions. Our results, displayed in Fig. 2a, indicate that an optimal interaction strength occurs at a tilt angle of  $\alpha = -22^\circ$ , which was therefore used in all following experiments.

Here, we measure EPI by imaging the transverse momentum distribution of the e-beam in High Dispersion Diffraction (HDD) mode using a 100-m camera length on a direct elec-

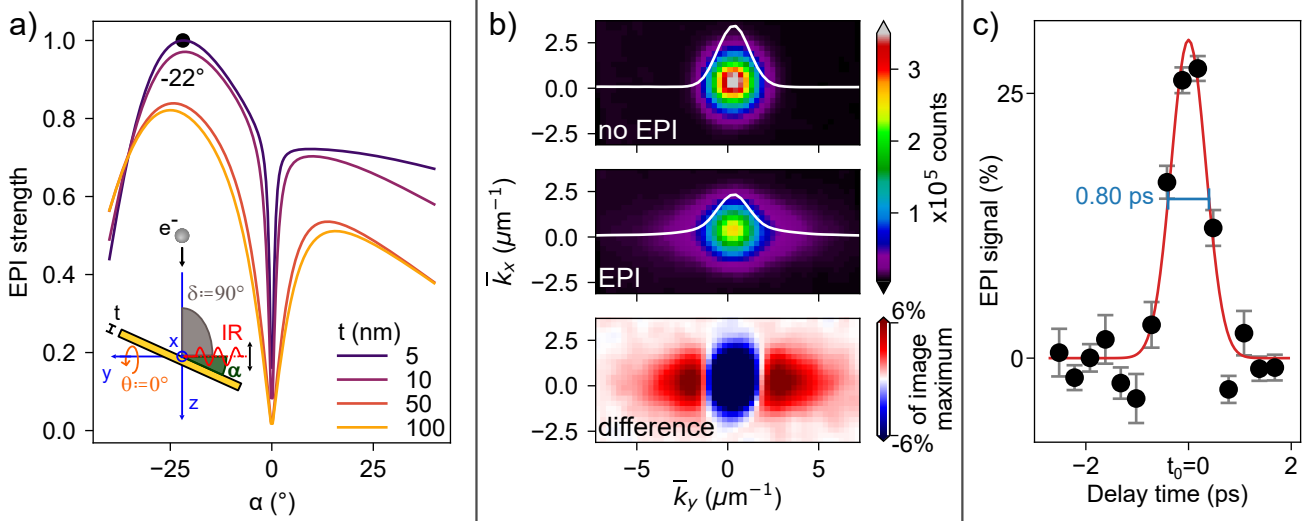


Figure 2: **Analysis of EPI at UniMiB.** **a)** Simulated interaction strength as a function of the gold-film tilt angle  $\alpha$ , accounting for non-perfect mirror conditions. The maximum EPI strength occurs at  $\alpha = -22^\circ$ , which is used in all subsequent measurements. The inset illustrates the experimental geometry of EPI at the PELM film. **b)** High Dispersion Diffraction (HDD) patterns of the e-beam under different conditions: without laser illumination (top panel), after interaction with IR photons (central panel), and their difference (lower panel). The interaction broadens the electron wave function along the  $k_y$  direction (laser propagation axis) and redistributes the intensity, reducing the signal near  $k = 0$  and increasing it at higher  $k_y$ . **c)** Temporal evolution of the EPI signal (defined in the main text) as a function of the laser-electron pulse delay. Black dots are data and red-solid line is a Gaussian fit. The extracted full width at half maximum (FWHM) is  $800 \pm 30$  fs. We define the temporal overlap  $t_0$  between the two pulses as the center of the Gaussian.

tron detector (see SI for further information). The large camera length is crucial to resolve small momentum transfers. Indeed, the interaction imparts discrete multiples of the light film-projected momentum  $k_L = (2\pi/\lambda) \cos^2(\alpha) = \frac{2\pi}{1030 \text{ nm}} \cos^2(22^\circ) \approx 5.2 \mu\text{m}^{-1}$  (see also SI), which is equivalent to an angular deflection of  $\theta \approx (k_\perp/k_\parallel) = k_L/(2\pi/\lambda_e) \approx 2.1 \mu\text{rad}$ , where  $\lambda_e \approx 2.5 \text{ pm}$  is the relativistic de Broglie wavelength for 200-keV electrons.

Figure 2b presents HDD momentum patterns of the e-beam under different conditions. In the absence of EPI (no light), the e-beam has a Gaussian momentum distribution (top panel). In the central panel, following interaction with IR photons, the electron wave function broadens along the  $k_y$ -axis, corresponding to the laser propagation direction<sup>31</sup> (see SI).

The lower panel in Fig. 2b displays the difference between the upper two panels, enhancing the contrast to clearly highlight the effect of EPI. The interaction reduces the electron signal

around  $k = 0$  while increasing it at higher  $k_y$  values. The absence of resolved stripes at multiples of  $k_L$  — as the ones shown in Fig. 4b — suggests that the transverse coherence length of the e-beam is on the order of the laser wavelength, limiting our ability to spatially resolve the quantum nature of the interaction.

We performed the experiment as a function of the delay time between laser and electron pulse to achieve a precise temporal overlap between the two ( $t_0$ : delay time = 0 ps). The results are shown in Fig. 2c. The EPI signal is represented by the depletion of the direct e-beam and we quantify it as  $1 - A_{\text{Voigt}}$ , where  $A_{\text{Voigt}}$  is the amplitude of a Voigt function fitted to the normalized  $k_y$ -integrated pattern. The temporal evolution of the EPI signal reveals a full width at half maximum (FWHM) of  $800 \pm 30$  fs, consistent with previous studies.<sup>2</sup>

Having demonstrated the ability to detect the effect of EPI on the electron wave function in momentum space at UniMiB, we per-

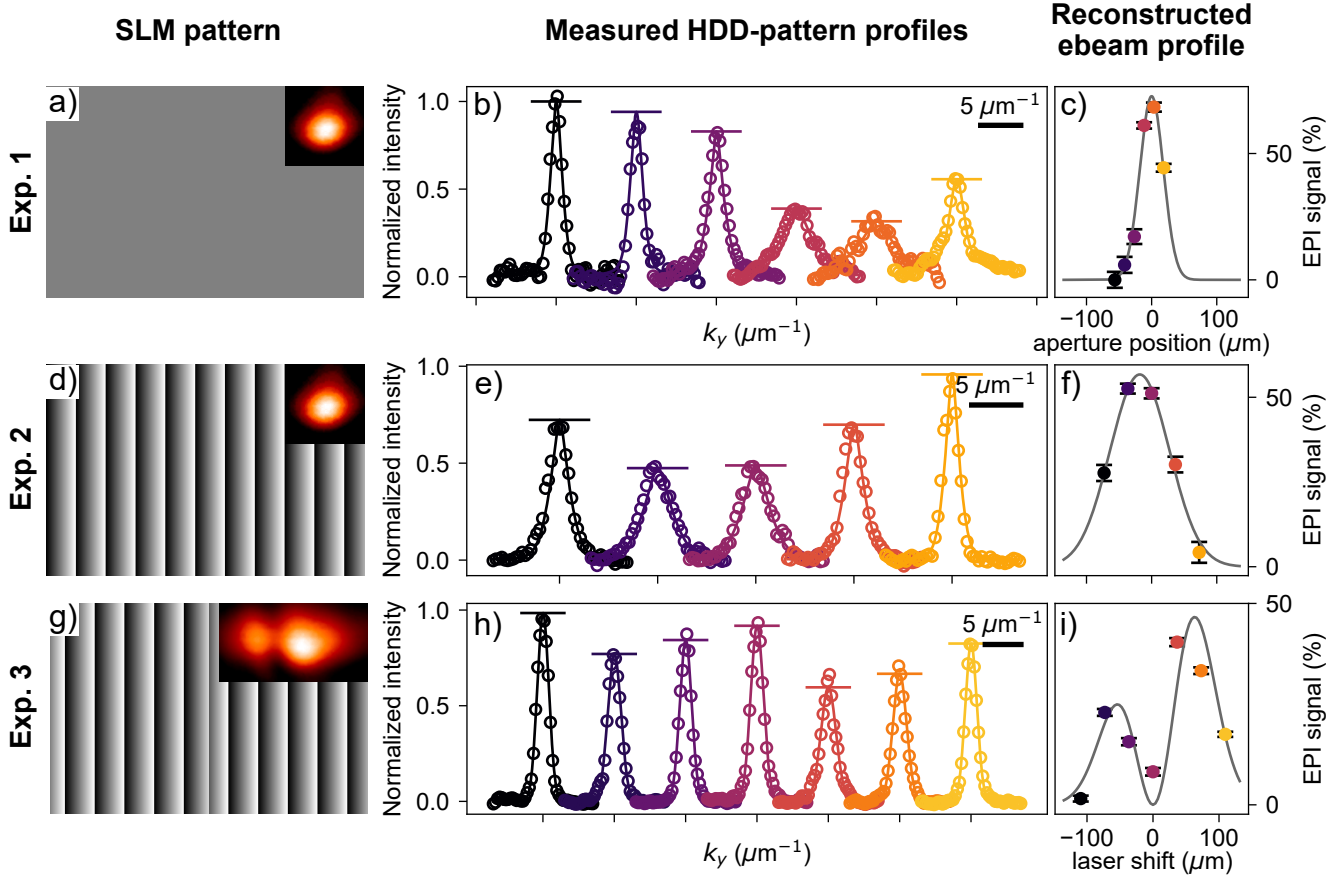


Figure 3: **Reconstruction of electron-beam transverse profiles at UniMiB.** **a,d,g)** patterns displayed by the SLM. The color scheme consist of a gray level of the pixels going from 0 to 255 to represent a laser phase shift from 0 to mod  $2\pi$ . The insets show the modulated laser transverse profile recorded with a CCD camera in the conjugate plane (see SI for further details on the experimental setup). **b,e,h)**  $k_x$ -integrated profiles (circles) of the HDD patterns acquired at maximum EPI. The colors represent different aperture positions (b) or laser shifts (e,h) coordinated with panels c,f,i). The curves are laterally shifted for clarity. Solid curves are Voigt-function fits while horizontal lines represent the fitted amplitudes  $A_{Voigt}$ . **c,f,i)** Electron-photon interaction (EPI) signal,  $1 - A_{Voigt}$ , as a function of the aperture position (c) or the laser shift (f,i)

formed 4D-STEM experiments to demonstrate transverse spatial modulation of the e-beam. In 4D-STEM, a focused e-beam is scanned across the sample while simultaneously capturing at each scan position a convergent-beam electron diffraction pattern, providing phase contrast analysis of the material under investigation.<sup>49,50</sup> Here, a focused light beam is scanned across the e-beam on the PELM film while simultaneously capturing at each scan position an HDD electron diffraction pattern (see also Fig. 1), providing transverse phase contrast analysis of the shaped e-beam.

Figure 3 illustrates the experiments con-

ducted with this 4D-STEM approach, with the electron and laser pulses in temporal overlap. A 20- $\mu\text{m}$  aperture (as the ones commonly used in a TEM column) is placed in the sample holder, downstream of the PELM stage (see Fig. 1). This aperture, smaller than the laser spot size, selects the electrons that interacted with a homogeneous portion of the electromagnetic field, condition needed for coherent interaction.<sup>33</sup> Electrons passing through the most intense regions of the laser beam interact with more photons, resulting in a stronger EPI signal, and vice versa.

The first row of Fig. 3 depicts the initial ex-

periment, in which the SLM serves as a simple mirror (pattern shown in panel a); the laser transverse profile is Gaussian, as shown in the inset. The aperture is scanned across this laser profile, and for each position, an HDD electron pattern is taken (as in Fig. 2b) before and at  $t_0$  (see Fig. 2c). The pre- $t_0$  images serve as reference to normalize the  $k_x$ -integrated profiles measured at maximum interaction. The resulting profiles, shown as circles in panel b, are fitted with a Voigt function (solid curves in panel b) and the fitted amplitudes are displayed as horizontal lines. Panel c shows the EPI signal,  $1 - A_{Voigt}$ , as a function of the aperture position, effectively reconstructing the e-beam profile at the aperture (sample) plane. We estimate the Gaussian-modulation diameter of the e-beam (at  $1/e^2$  intensity) to be approximately  $72 \pm 5 \mu\text{m}$ .

The second row of Fig. 3 presents a similar experiment where the aperture remains fixed while the laser beam is scanned across the PELM film using the SLM. In this case, a blazed grating (shown in panel d) is employed to shift the laser beam in a controlled manner, based on the diffraction condition for the first order:  $\Delta\delta = \lambda\Delta n/H$ . Here,  $\Delta\delta$  is the laser tilt change,  $H$  is the SLM horizontal dimension and  $\Delta n$  is the difference in the number of grating periods, which is varied to scan the laser on the PELM stage (see also SI). From these calculations, we can estimate the Gaussian modulation diameter at the PELM plane to have a  $1/e^2$ -diameter of  $180 \pm 20 \mu\text{m}$ . By comparing panel f with panel c, we deduce that the e-beam has been de-magnified by a factor 2.5 between the PELM and the sample plane, consistent with the almost-parallel configuration of the e-beam post-PELM (see SI) and verifying that experiment 1 and experiment 2 give the same result.

The third row of Fig. 3 depicts a further variation of the experiment, using a different SLM pattern. Here, a horizontal phase shift is superimposed on the blazed grating pattern (panel g), producing a two-lobed Hermite-Gaussian profile  $\text{HG}_{01}$  in the far field, as shown in the inset of panel g. The integrated HDD patterns in panel h allow reconstruction of the e-beam

profile (panel i), which mirrors the two-lobed shape imparted by the light beam.

Our results clearly demonstrate the ability to manipulate the e-beam prior to sample interaction and to observe the resulting modulations at the sample plane. These findings demonstrate that such a PELM device is now ready for performing ultrafast measurements with a shaped e-beam on real samples. Furthermore, our system demonstrates versatility, not only in e-beam shaping but also in e-beam demagnification, as we have shown by reducing the e-beam pattern by a factor of 2.5, with further scalability possible.

### Longitudinal modulation

Influencing the longitudinal phase of the e-beam requires temporal modification of its single-particle wave function. Because time modification beyond free evolution directly implies modification of the energy spectrum, we can access the electron longitudinal phase shift via direct imaging in the energy domain. From a technological point of view, appropriate time-dependent optical fields, as obtained via OPAs (used in this work), two-wave mixing, or DLAs, are needed in order to achieve the desired modulation.

At Technion, we achieve light-induced longitudinal e-beam modulation by exploiting inelastic EPI via ITR, which is mediated by a 30-nm-thick Aluminum film deposited on a 40-nm  $\text{Si}_3\text{N}_4$  membrane. In this case, the metallic film closely behaves as a perfect mirror.

For longitudinal modulation to be adopted in imaging, it is crucial that the light field imprints the same phase shift at every transverse position of the electron wave function. In order to assure exact phase matching at the PELM plane between electrons and light interacting at the PELM-film interface, the film is tilted by an angle  $\gamma = 40.9^\circ$  with respect to the horizontal plane (shown in Fig. 4a). This angle can be obtained as:  $\tan(\gamma) = \sin\delta/(c/v - \cos\delta)$ , where  $\delta$  is the angle between the electron and light (fixed at  $70^\circ$ ),  $c$  is the light speed and  $v$  is the electron speed ( $v = 0.7c$  at 200 keV). Such expression is derived by imposing that the



phase shift experienced by the electron pulse while interacting with the light field ( $\Delta\Phi_e = (\omega\Delta z/v) \sin\gamma$ , where  $\Delta z$  is the interaction distance), is equal to the projected phase of the light pulse on the PELM-film surface ( $\Delta\Phi_L = -\Delta z \frac{\omega}{c} \cos(\pi/2 - \delta + \gamma)$ ). This condition makes sure that a spatially-uniform longitudinal phase profile is imprinted on the electron wave function at the PELM plane.

Here, we measure EPI by monitoring the energy distribution of the e-beam via the acquisition of either energy-resolved spectra or energy-filtered images.

In Figs. 4 and 5 we show the results of the simultaneous illumination of two Al/Si<sub>3</sub>N<sub>4</sub> films, one placed at the PELM plane and tilted by  $\gamma = 40.9^\circ$ , and the other one placed at the sample plane with a variable tilting angle. Such configuration results in two subsequent EPIs both governed by ITR mechanism.

In Fig. 4b we observe the effect of such double interaction in the energy-time dimensions. Electron energy loss spectra are measured as a function of the delay time,  $\Delta t$ , between the modulation pulse and the pump pulse, while keeping the electron pulse and the light pulse at the sample always at their optimal temporal overlap. At  $\Delta t$  values very different from zero (black linecut in Fig. 4c), the spectrum shows multiple quantized energy exchanges on both sides of the zero-loss peak (ZLP) as a result of EPI only at the sample stage. However, while approaching the optimal temporal overlap also between electron and light pulses at the PELM stage (red linecut), a stronger modulation across the spectrum is observed especially in energy regions far away from the ZLP.

A direct evidence of the coherent phase modulation experienced by the electron wave packet can be obtained via energy-filtering imaging of the spatial distribution of the e-beam following such double interaction. In Fig. 5 we present the results of such imaging experiments, where energy-filtered images have been acquired as a function of the tilting angle of the sample film while maintaining optimal temporal overlap between electrons and light at both PELM and sample stages. Here, it is possible to observe the formation of a series of spatial fringes induced

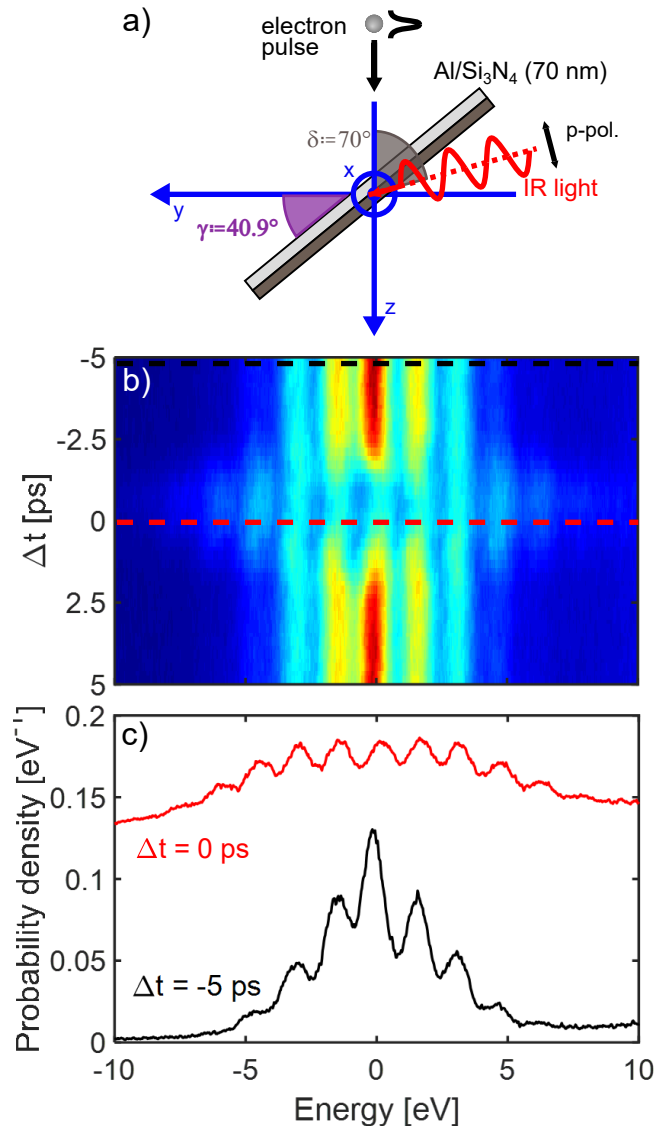


Figure 4: **a)** Experimental geometry of EPI at the PELM film. **b)** Electron energy spectra versus PELM time-delay taken while the sample laser is at optimal temporal overlap, thus demonstrating *double* EPI. **c)** Cross-sections taken from the data in panel a along the color-coordinated dashed lines, showing the EPI spectra at  $\Delta t = -5$  ps (only sample EPI), and  $\Delta t = 0$  ps (both sample and PELM EPI).

by the coherent superposition of the electron wave functions modulated by the two interaction points (PELM and sample). The periodicity of the fringes depends on the projection of the light wave vector on the tilted sample film and thus strongly changes when varying the sample tilting angle.

The short separation between the PELM po-



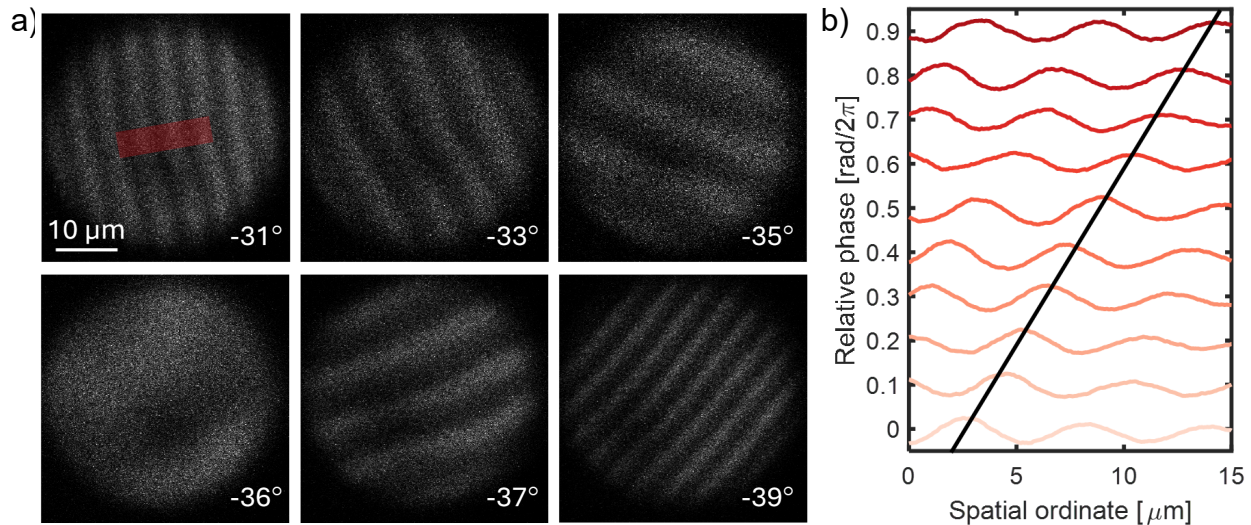


Figure 5: **a**) Electron interferograms obtained by recording energy-filtered TEM images for different sample tilt angles, and at optimal temporal overlap at both the PELM and the sample. Sample tilt angle is indicated for each panel. The bottom-left panel ( $-36^\circ$ ) shows near-perfect phase matching (0 to  $2\pi$  phase modulation across the ROI). **b**) Cross-sections of an interferogram, similar to those shown in **a**, taken while sweeping the relative PELM-sample time-delay (or phase) across a full optical period (2.73 fs). The black line traces the position of one peak for varying delays. By recording such a phase series for each sample time delay, one can reconstruct the complete spatiotemporal phase profile of the electric field. The red rectangle in the top-left panel of **a** illustrates the ROI used to draw the cross-sections in **b**.

sition and the sample position is ideal for dispersive reshaping of the electron pulse to obtain attosecond longitudinal modulation of the beam in a Ramsey-like setup.<sup>15,39,51</sup> In this respect it is crucial to have a precise correlation between the phase shift imprinted on the electron wave function and the relative phase difference between the two light pulses, the one driving the e-beam modulation and the other driving the sample excitation. In Fig. 5a we show electron interferograms measured at a given sample tilting angle as a function of the delay time  $\Delta t$  between the PELM laser and the pump (sample) laser within a single optical cycle. At each delay time, the measured shift of the electron fringes in the energy-filtered images is correlated with the optical phase difference (Fig. 5b) as measured via a Mach-Zender interferometer. The latter is shown in details in Fig. S6b of the SI: the laser beams directed at the PELM and sample planes are further separated and delayed with respect to each other before arriving on a CCD camera, where optical interference is recorded. From the mea-

surements, we clearly observe a strong correlation between the optical phase and the electron phase, confirming that the PELM device is properly behaving.

## Conclusions

In conclusion, we have successfully integrated a PELM device into the UTEMs at UniMiB and Technion, enabling on-demand control over the electron wave function in both longitudinal and transverse directions. This was achieved through the integration of an additional EPI stage within the TEM column, allowing for e-beam modulation before the sample plane. This novel configuration expands the possibilities for using shaped e-beams in ultrafast electron microscopy experiments.

Given the capabilities of tailored e-beam shaping, PELM-equipped UTEMs open up new avenues for image-resolution enhancements, selective probing, and low-dose imaging. In particular, potential applications include single-

pixel electron imaging, where a high number of patterns have to be imprinted on the electron wave function to obtain high-resolution images with minimal electron dose.<sup>37</sup> This capability could revolutionize imaging techniques, making the PELM system an essential tool for the next generation of ultrafast electron microscopy studies.

## Associated content

The Supporting Information provides detailed technical descriptions and geometry of the UTEM setup at the University of Milano-Bicocca, including the phase-modulating Spatial Light Modulator. Calibration procedures for lens configurations (e.g., C<sub>0</sub> and C<sub>3</sub> lenses) and electron beam coherence optimization are explained, alongside calculations for camera length and momentum transfer during electron-photon interactions. The document also describes the role of apertures in controlling beam coherence and intensity, compares pre- and post-condenser lens PELM configurations, and discusses simulations using STEMCELL software to analyze electron beam properties. Additional setups, such as the Technion UTEM, and synchronization techniques for pump-probe experiments are briefly covered.

## Acknowledgments

B.M.F. thanks V. Di Giulio and K. Beeks for insightful conversations. We thank J.-C. Olaya and A. Hermerschmidt from HOLOEYE for their technical support with the SLM. This work is part of the SMART-electron project that has received funding from the European Union's Horizon 2020 Research and Innovation Programme under Grant Agreement No 964591.

## References

- (1) Vanacore, G.; Fitzpatrick, A.; Zewail, A. Ultrafast Imaging, Diffraction and Spectroscopy in Materials Science and Biology. *Nano Today* **2016**, *11*, 228–249.
- (2) Barwick, B.; Zewail, A. H. Photonics and Plasmonics in 4D Ultrafast Electron Microscopy. *ACS Photonics* **2015**, *2*, 1391–1402.
- (3) Zewail, A. H. Four-Dimensional Electron Microscopy. *Science* **2010**, *328*, 187–193.
- (4) Arbouet, A.; Caruso, G. M.; Houdellier, F. In *Advances in Imaging and Electron Physics*; Hawkes, P. W., Ed.; Advances in Imaging and Electron Physics; Elsevier, 2018; Vol. 207; pp 1–72.
- (5) Büttner, F. et al. Observation of Fluctuation-Mediated Picosecond Nucleation of a Topological Phase. *Nature Materials* **2021**, *20*, 30–37.
- (6) Domröse, T.; Fernandez, N.; Eckel, C.; Rosnagel, K.; Weitz, R. T.; Ropers, C. Nanoscale Operando Imaging of Electrically Driven Charge-Density Wave Phase Transitions. *Nano Letters* **2024**, *24*, 12476–12485.
- (7) Truc, B.; Sapozhnik, A. A.; Tengdin, P.; Viñas Boström, E.; Schönenberger, T.; Gargiulo, S.; Madan, I.; LaGrange, T.; Magrez, A.; Verdozzi, C.; Rubio, A.; Rønnow, H. M.; Carbone, F. Light-Induced Metastable Hidden Skyrmion Phase in the Mott Insulator Cu<sub>2</sub>OSeO<sub>3</sub>. *Advanced Materials* **2023**, *35*, 2304197.
- (8) Ungeheuer, A.; Bach, N.; Mir, M. T.; Hasaniien, A. S.; Nöding, L.; Baumert, T.; Schäfer, S.; Senftleben, A. Coherent Acoustic Phonons in a Coupled Hexagonal Boron Nitride–Graphite Heterostructure. *Structural Dynamics* **2024**, *11*, 014501.
- (9) Tauchert, S. R.; Volkov, M.; Ehberger, D.; Kazenwadel, D.; Evers, M.; Lange, H.; Donges, A.; Book, A.; Kreuzpaintner, W.; Nowak, U.; Baum, P. Polarized Phonons Carry Angular Momentum in Ultrafast

- Demagnetization. *Nature* **2022**, *602*, 73–77.
- (10) Kazenwadel, D.; Neathery, N.; Prakash, S.; Ariando, A.; Baum, P. Cooling Times in Femtosecond Pump-Probe Experiments of Phase Transitions with Latent Heat. *Physical Review Research* **2023**, *5*, 043077.
- (11) Aguilar, F.; Lourenço-Martins, H.; Montero, D.; Li, X.; Kociak, M.; Campos, A. Selective Probing of Longitudinal and Transverse Plasmon Modes with Electron Phase-Matching. *The Journal of Physical Chemistry C* **2023**, *127*, 22252–22264.
- (12) Woo, S. Y. et al. Engineering 2D Material Exciton Line Shape with Graphene/h-BN Encapsulation. *Nano Letters* **2024**, *24*, 3678–3685.
- (13) Vanacore, G. M.; Madan, I.; Carbone, F. Spatio-Temporal Shaping of a Free-Electron Wave Function via Coherent Light–Electron Interaction. *La Rivista del Nuovo Cimento* **2020**, *43*, 567–597.
- (14) Madan, I.; Vanacore, G. M.; Gargiulo, S.; LaGrange, T.; Carbone, F. The Quantum Future of Microscopy: Wave Function Engineering of Electrons, Ions, and Nuclei. *Applied Physics Letters* **2020**, *116*, 230502.
- (15) Bucher, T. et al. Coherently Amplified Ultrafast Imaging Using a Free-Electron Interferometer. *Nature Photonics* **2024**, *18*, 809–815.
- (16) Kozák, M.; Eckstein, T.; Schönenberger, N.; Hommelhoff, P. Inelastic Ponderomotive Scattering of Electrons at a High-Intensity Optical Travelling Wave in Vacuum. *Nature Physics* **2018**, *14*, 121–125.
- (17) Adiv, Y.; Wang, K.; Dahan, R.; Broadus, P.; Miao, Y.; Black, D.; Leedle, K.; Byer, R. L.; Solgaard, O.; England, R. J.; Kaminer, I. Quantum Nature of Dielectric Laser Accelerators. *Physical Review X* **2021**, *11*, 041042.
- (18) Madan, I.; Leccese, V.; Mazur, A.; Barantani, F.; LaGrange, T.; Sapozhnik, A.; Tengdin, P. M.; Gargiulo, S.; Rotunno, E.; Olaya, J.-C.; Kaminer, I.; Grillo, V.; García de Abajo, F. J.; Carbone, F.; Vanacore, G. M. Ultrafast Transverse Modulation of Free Electrons by Interaction with Shaped Optical Fields. *ACS Photonics* **2022**, *9*, 3215–3224.
- (19) Chirita Mihaila, M. C.; Weber, P.; Schneller, M.; Grandits, L.; Nimmrichter, S.; Juffmann, T. Transverse Electron-Beam Shaping with Light. *Physical Review X* **2022**, *12*, 031043.
- (20) Vanacore, G. M.; Berruto, G.; Madan, I.; Pomarico, E.; Biagioni, P.; Lamb, R. J.; McGrouther, D.; Reinhardt, O.; Kaminer, I.; Barwick, B.; Larocque, H.; Grillo, V.; Karimi, E.; García de Abajo, F. J.; Carbone, F. Ultrafast Generation and Control of an Electron Vortex Beam via Chiral Plasmonic near Fields. *Nature Materials* **2019**, *18*, 573–579.
- (21) Tsesses, S.; Dahan, R.; Wang, K.; Bucher, T.; Cohen, K.; Reinhardt, O.; Bartal, G.; Kaminer, I. Tunable Photon-Induced Spatial Modulation of Free Electrons. *Nature Materials* **2023**, *22*, 345–352.
- (22) Schwartz, O.; Axelrod, J. J.; Campbell, S. L.; Turnbaugh, C.; Glaeser, R. M.; Müller, H. Laser Phase Plate for Transmission Electron Microscopy. *Nature Methods* **2019**, *16*, 1016–1020.
- (23) Kozák, M.; Schönenberger, N.; Hommelhoff, P. Ponderomotive Generation and Detection of Attosecond Free-Electron Pulse Trains. *Physical Review Letters* **2018**, *120*, 103203.
- (24) García de Abajo, F. J.; Konečná, A. Optical Modulation of Electron Beams in Free

- Space. *Physical Review Letters* **2021**, *126*, 123901.
- (25) Barwick, B.; Flannigan, D. J.; Zewail, A. H. Photon-Induced near-Field Electron Microscopy. *Nature* **2009**, *462*, 902–906.
- (26) García de Abajo, F. J.; Asenjo-Garcia, A.; Kociak, M. Multiphoton Absorption and Emission by Interaction of Swift Electrons with Evanescent Light Fields. *Nano Letters* **2010**, *10*, 1859–1863.
- (27) Park, S. T.; Lin, M.; Zewail, A. H. Photon-Induced near-Field Electron Microscopy (PINEM): Theoretical and Experimental. *New Journal of Physics* **2010**, *12*, 123028.
- (28) Steinhauer, L. C.; Romea, R. D.; Kimura, W. D. Inverse Transition Radiation. The Seventh Workshop on Advanced Accelerator Concepts. Lake Tahoe, California (USA), 1997; pp 673–686.
- (29) Weingartshofer, A.; Holmes, J. K.; Caudle, G.; Clarke, E. M.; Krüger, H. Direct Observation of Multiphoton Processes in Laser-Induced Free-Free Transitions. *Physical Review Letters* **1977**, *39*, 269–270.
- (30) Plettner, T.; Byer, R. L.; Colby, E.; Cowan, B.; Sears, C. M. S.; Spencer, J. E.; Siemann, R. H. Visible-Laser Acceleration of Relativistic Electrons in a Semi-Infinite Vacuum. *Physical Review Letters* **2005**, *95*, 134801.
- (31) Vanacore, G. M.; Madan, I.; Berruto, G.; Wang, K.; Pomarico, E.; Lamb, R. J.; McGrouther, D.; Kaminer, I.; Barwick, B.; García de Abajo, F. J.; Carbone, F. Attosecond Coherent Control of Free-Electron Wave Functions Using Semi-Infinite Light Fields. *Nature Communications* **2018**, *9*, 2694.
- (32) Morimoto, Y.; Baum, P. Diffraction and Microscopy with Attosecond Electron Pulse Trains. *Nature Physics* **2018**, *14*, 252–256.
- (33) Feist, A.; Yalunin, S. V.; Schäfer, S.; Ropers, C. High-Purity Free-Electron Momentum States Prepared by Three-Dimensional Optical Phase Modulation. *Physical Review Research* **2020**, *2*, 043227.
- (34) Wang, W.; Zheng, D.; Huang, S.; Li, J.; Zhang, Y.; Miao, T.; Sun, S.; Tian, H.; Yang, H.; Li, J. Energy-Momentum Transfer in the Free-Electron–Photon Interaction Mediated by a Film. *Physical Review B* **2024**, *109*, 134305.
- (35) Fang, Y.; Kuttruff, J.; Nabben, D.; Baum, P. Structured Electrons with Chiral Mass and Charge. *Science* **2024**, *385*, 183–187.
- (36) Glauber, R. J.; Lewenstein, M. Quantum Optics of Dielectric Media. *Physical Review A* **1991**, *43*, 467–491.
- (37) Konečná, A.; Rotunno, E.; Grillo, V.; García De Abajo, F. J.; Vanacore, G. M. Single-Pixel Imaging in Space and Time with Optically Modulated Free Electrons. *ACS Photonics* **2023**, *10*, 1463–1472.
- (38) Mattes, M.; Volkov, M.; Baum, P. Femtosecond Electron Beam Probe of Ultrafast Electronics. *Nature Communications* **2024**, *15*, 1743.
- (39) Gaida, J. H.; Lourenço-Martins, H.; Sivis, M.; Rittmann, T.; Feist, A.; García de Abajo, F. J.; Ropers, C. Attosecond Electron Microscopy by Free-Electron Homodyne Detection. *Nature Photonics* **2024**, *18*, 509–515.
- (40) Giulio, V. D.; Kociak, M.; García de Abajo, F. J. Probing Quantum Optical Excitations with Fast Electrons. *Optica* **2019**, *6*, 1524–1534.
- (41) Yang, Y.; Cattaneo, P.; Raja, A. S.; Weaver, B.; Wang, R. N.; Sapozhnik, A.; Carbone, F.; LaGrange, T.; Kippenberg, T. J. Unifying Frequency Metrology across Microwave, Optical, and Free-Electron Domains. 2024.

- (42) Baum, P. On the Physics of Ultrashort Single-Electron Pulses for Time-Resolved Microscopy and Diffraction. *Chemical Physics* **2013**, *423*, 55–61.
- (43) Fowles, G. R. *Introduction to Modern Optics*, 2nd ed.; Dover Publications: New York, 1989.
- (44) Janzen, A.; Krenzer, B.; Heinz, O.; Zhou, P.; Thien, D.; Hanisch, A.; Meyer Zu Heringdorf, F.-J.; Von Der Linde, D.; Horn Von Hoegen, M. A Pulsed Electron Gun for Ultrafast Electron Diffraction at Surfaces. *Review of Scientific Instruments* **2007**, *78*.
- (45) Kirchner, F. O.; Lahme, S.; Krausz, F.; Baum, P. Coherence of Femtosecond Single Electrons Exceeds Biomolecular Dimensions. *New Journal of Physics* **2013**, *15*, 063021.
- (46) Gahlmann, A.; Park, S. T.; Zewail, A. H. Ultrashort Electron Pulses for Diffraction, Crystallography and Microscopy: Theoretical and Experimental Resolutions. *Physical Chemistry Chemical Physics* **2008**, *10*, 2894–2909.
- (47) Grillo, V.; Rotunno, E. STEM\_CELL: A Software Tool for Electron Microscopy: Part I—Simulations. *Ultramicroscopy* **2013**, *125*, 97–111.
- (48) Grillo, V.; Rossi, F. STEM\_CELL: A Software Tool for Electron Microscopy. Part 2 Analysis of Crystalline Materials. *Ultramicroscopy* **2013**, *125*, 112–129.
- (49) Ophus, C. Four-Dimensional Scanning Transmission Electron Microscopy (4D-STEM): From Scanning Nanodiffraction to Ptychography and Beyond. *Microscopy and Microanalysis* **2019**, *25*, 563–582.
- (50) Koutenský, P.; Streshkova, N. L.; Moriová, K.; Mihaila, M. C. C.; Burda, D.; Knápek, A.; Kozák, M. Ultrafast 4D scanning transmission electron microscopy for imaging of localized optical fields. 2025; <http://arxiv.org/abs/2502.07338>, arXiv:2502.07338 [physics].
- (51) Nabben, D.; Kuttruff, J.; Stolz, L.; Ryabov, A.; Baum, P. Attosecond Electron Microscopy of Sub-Cycle Optical Dynamics. *Nature* **2023**, *619*, 63–67.